Engineering Structures 250 (2022) 113285

Contents lists available at ScienceDirect

Engineering Structures

journal homepage: www.elsevier.com/locate/engstruct

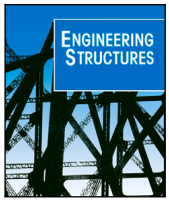

Précis of gap test results requiring reappraisal of line crack and phase-field models of fracture mechanics

Zdeněk P. Bažant [a,*], A. Abdullah Dönmez [b,c], Hoang T. Nguyen [c]

[a] McCormick Institute Professor and W.P. Murphy Professor of Civil and Mechanical Engineering and Materials Science, Northwestern University, 2145 Sheridan Road, CEE/A135, Evanston, IL 60208, United States of America
[b] Istanbul Technical University, Turkey
[c] Northwestern University, United States of America

ARTICLE INFO

In honor of Professor Herbert Mang at the occasion of his 80th birthday

Keywords:
Fracture mechanics, Crack-parallel stresses
T-stress
Cohesive crack model, Crack band model, Nonlocal models
Material characteristic length
Fracture testing
Concrete
Quasibrittle behavior
Fracture process zone
XFEM
Phase-field models
Yielding zone

ABSTRACT

This paper presents a brief review of the recent advances in fracture mechanics at Northwestern University and Istanbul Technical University, prompted by the recent discovery of the gap test—a test that makes it easy and unambiguous to determine the effects of crack-parallel stresses on the mode-I fracture energy and, in consequence, on the nominal strength of structures of different sizes (aka, the size effect). The standard fracture specimens cannot reveal these effects since they have zero or negligible crack-parallel stresses. In addition, these effects cannot be reproduced by the standard, widely used, fracture models including the linear elastic fracture mechanics (LEFM), the cohesive crack model (CCM), as well as the popular computational models such as the extended finite element (XFEM) and the phase-field models (PFM). Therefore, it will be necessary to adopt fracture models that can reflect the tensorial damage behavior in the fracture process zone (FPZ), which is governed by at least two characteristic lengths, one for the FPZ length and one for the FPZ width. The modeling of elasto-plastic metals is even more complicated since the FPZ of micrometer-scale width is surrounded by a millimeter-scale plastic-hardening (yielding) zone. This role of the yielding zone has been understood well since the 1980s except for the scaling laws which are helpful for determining the effect of crack-parallel stresses more accurately. As a general conclusion, the line crack and phase field models cannot be used for practical problems with significant crack-parallel stress components ($\sigma_{xx}, \sigma_{zz}, \sigma_{xz}$). However, thanks to the finite width of its fracture front, the crack band model can be used, provided that its tensorial damage law is realistic. A new challenge for the nonlocal and gradient models is that they, too, will need to distinguish two independent material characteristic lengths, one for the direction of damage band and one transverse to it.

1. Introduction

Although an effect of the crack-parallel stresses on the fracture of concrete and other quasibrittle materials has been suspected since the 1980s, little [1] or no clear information existed until the 2020 discovery [2,3] of the simple gap test, in which crack-parallel compression or tension at the fracture front can be easily produced and controlled. Using elastic-perfectly plastic loading pads, the standard notched three-point-bend beam is first loaded by compression parallel to the notch while the end supports are installed with a suitable gap such that they engage only after a constant plastic plateau in the pads is reached. Upon testing scaled beams of several sizes, the fracture energy is evaluated by the size effect method. In the Hutchinson–Rice–Rosengren (HRR) theory [4,5] for the plastic-hardening fracture of metals, the way the normal stress σ_{xx} in the propagation direction, called the T-stress, affects the FPZ of micrometer-scale width is complicated by the surrounding yielding zone of millimeter-scale width. This effect was in essence clarified in the 1990s [6,7]. However, the scaling law useful for evaluating the standard fracture tests was not established until 2021 [8]. Here, eschewing mathematical details, we present a succinct overview of the recent studies conducted at Northwestern University and Istanbul Technical University. Finally, we point out the need for a reappraisal of fracture mechanics.

In fracture modeling of concrete and other non-metallic materials, the effect of crack-parallel stresses has generally been ignored. The explanation is that, in the line-crack model such as the linear elastic fracture mechanics (LEFM) and the cohesive crack model (CCM), a line cut along the direction of a uniform uniaxial stress field produces

* Corresponding author.
E-mail address: z-bazant@northwestern.edu (Z.P. Bažant).

https://doi.org/10.1016/j.engstruct.2021.113285

Available online 3 November 2021

no stress change. This also explains why all the standard fracture test specimens – three-point-bend (3PB), compact tension (CT), single-edge-notched tension (SENT), circumferentially notched tension (CNT), diametral compression (DC), edge-notched eccentric compression, and double cantilever beam (DCB) – have zero or almost zero crack-parallel stresses. It might seem that the wedge-splitting specimen studied by Tschegg [9] was an exception, but its crack-parallel compression is too small compared to the uniaxial compression strength, f_c, and its field is nonuniform, with a maximum occurring away from the FPZ.

The effect of crack-parallel stress σ_{xx} in the propagation direction, called the T-stress, and particularly the way it interferes with the yielding zone, was carefully studied in the context of the HRR theory [4,5] of plastic-hardening metals [6,7,10–12], as reviewed in detail in [8]. The T-stress effect was also analyzed in [13], but it was in the context of lateral deflection of the crack path in LEFM.

2. Gap tests of concrete and their evaluation

An advantage of the gap test, depicted in Fig. 1a, is its simplicity and evaluation unambiguity. This is thanks to the fact that, upon closing the gaps at the beam ends, the support system transits from one statically determinate configuration to another.

Another advantage is that the plastic pads produce a field of nearly uniform uniaxial compression around the FPZ.

The third advantage is that the fracture energy G_f can be easily measured by the size effect method which is simple and has a relatively low experimental error [14,15].

For concrete, the plastic pads made of polypropylene have been used, while, for aluminum, pads of polyvinyl chloride (PVC) became necessary to provide a larger T-stress. The crack-tip opening displacement δ_{CTOD} is controlled by an extensometer (Fig. 1b). Geometrically similar specimens of several sufficiently different sizes are tested. The size effect law [16] is utilized, in which case it suffices to measure only the peak loads. This is the most robust test of both the initial fracture energy G_f and the effective fracture process zone size c_f. It has been adopted as an international standard recommendation of RILEM [17] and was endorsed by the ACI-446 committee. Another advantage of the size effect method is that it is reducible to linear regression (in detail see [2,3]).

The experimental results shown in Fig. 2 were obtained with normal concrete of maximum aggregate size 18 mm and a mean cylindrical compressive strength $f_c = 40.5$ MPa. The geometry is defined by the span-to-depth ratio $2L/D = 3.75$ and the notch depth ratio $a/D = 0.3$. The depths of geometrically scaled beams were $D = 101.6$ mm (4 in), 203.2 mm (8 in), and 406.4 mm (16 in). The data points (empty circles) in Fig. 2a are the measured values of fracture energy G_f for different levels of compression stress σ_{pad} applied at the yielding pads.

Note that G_f and c_f depends strongly on the compressive stress, σ_{pad}, at the pads. This shows that both the LEFM, which can be implemented via the extended finite element method (XFEM), and the phase-field models (PFM) as well as the CCM, are inapplicable. The stress σ_{xx} near the notch tip, which represents a material property, is only slightly different from σ_{pad} and is in Fig. 2a,b shown by the solid circle points.

As expected, the test results could be closely matched by the finite element (FE) crack band model [18–20], which has become the most widely used fracture model used in the practice of concrete and geomaterials, as well as in composite airframe design. In this model, the width, h, of the fracture front is considered to be a material fracture property; $h = G_{f0}/A$ where A = area under the stress-mean transverse strain curve and $G_{f0} = G_f$ value for $\sigma_{xx} = 0$. A realistic tensorial damage law must be used in the crack band model, and concrete microplane model M7 [21,22] has been adopted for this purpose (it was implemented as user-defined material in ABAQUS).

The crack band model results are marked in Fig. 2a,b by solid and dashed curves. The decrease of G_f at high compression is represented well. The increase of G_f at moderate compression is underestimated, although the overall trend is correct. The underestimation could be eliminated by noting that the widening of the FPZ calls for increasing the finite element width at the crack band front. This would be computationally difficult, but the increase of G_f can alternatively be represented by adjustment of the postpeak softening in model M7. However, such adjustment can only be justified if the change of G_f does not depend on the loading path, which was shown not to be the case in [3].

To provide an intuitive physical explanation of the G_f variation, consider the schematic picture in Fig. 3a. The initial rising part of the curve in Fig. 2a is explained by a σ_{xx}-generated increase of static friction (and aggregate interlock) on microcracks (and microplanes) inclined with respect to the directions of macrocrack propagation [23]. To explain the subsequent descending part of the curve, a further increase of crack-parallel compression must overcome friction and cause slip on the inclined microcracks. This must lead to lateral expansion of the FPZ and, thereby, to axial splitting cracks (Fig. 3a) which tend to widen the FPZ [24]. Such behavior is not predicted by the classical Drucker–Prager and Mohr–Coulomb plasticity models. This comes as no surprise since the plasticity-type failure criteria based on tensor invariants cannot capture oriented phenomena such as slip on planes of distinct orientation, which are the reality.

Parameter c_f of the size effect law obtained by fitting the gap tests of various sizes also varies with the crack-parallel compression σ_{xx}; see Fig. 2b. This, too, is captured in essence by the simulations with the crack band model and M7, although the c_f-increase at moderate crack-parallel compression is again underestimated. This increase and the underestimation of G_f at moderate crack-parallel stress calls for an increase of crack band width h. Indeed, such an increase would cancel the underestimations of both G_f and c_f, but will be difficult to characterize computationally. An equivalent increase via M7 is nevertheless possible

The foregoing observations have further serious consequences for the nonlocal and gradient models. They indicate that the nonlocal material characteristic length l_0 should not be kept constant but should vary as a function of the normal stress in the principal direction of the damage tensor in the developing damage localization band that terminates in fracture.

Furthermore, it appears that the difference between the M7 prediction and the maximum data point in Fig. 2a is not due to the damage constitutive law. This implies that the material characteristic length for the width of the FPZ (though not that for the length of FPZ) should depend on the crack-parallel stress, which is also supported by the physical cause of changing FPZ width proposed in Fig. 2c. This calls for an improvement in the crack band models and is a major challenge for the nonlocal and gradient models of material damage.

Also noteworthy are the crack band M7 simulations in Fig. 2. They indicate that the crack-parallel stress effect is highly path dependent. Different loading sequences leading to the same combination of crack-parallel stress and stress intensity factor yield very different failure predictions. This means that, in computations, it would be insufficient to vary the G_f-value based on the current stress state (see Fig. 3b). The effective G_f is strongly path-dependent.

In [2,3], it was further predicted, by appropriate crack-band microplane simulations, that similar effects occur in fiber reinforced concrete and in shale ([3, Fig. 8]). Experimental confirmation is still pending.

3. T-Stress effect and scaling of the HRR theory of metal fracture

While polycrystalline metals have a simpler microstructure than concrete, the scaling of their strength is complicated by a relatively large, millimeter scale, yielding zone of plastic hardening metal, which surrounds a far narrower, micrometer scale, FPZ. In consequence, as shown in [8], the law of size effect must reproduce not one but two

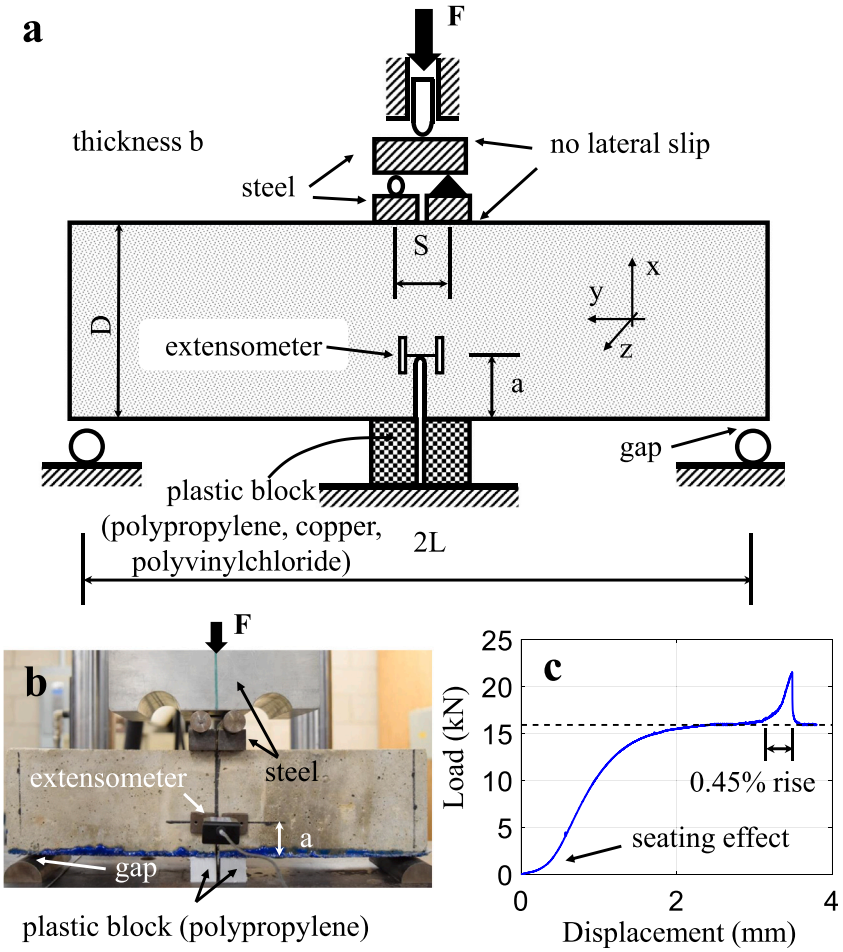

Fig. 1. **a.** Schematic of gap test; **b.** Concrete beam set up for gap test of notched concrete beam of depth 101.6 mm (4 in.); **c.** Load–deflection diagram, in which a spike, rising from the plateau, is due to bending moment applied from end supports after their engagement.

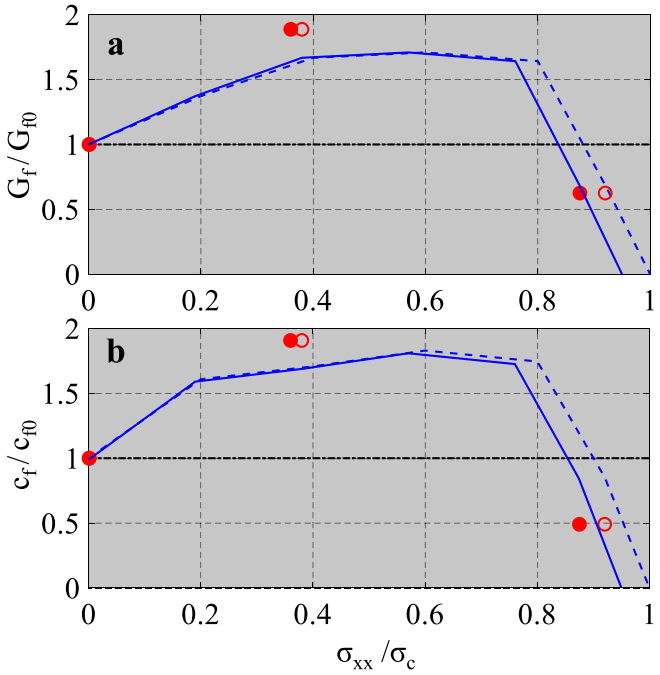

Fig. 2. Gap test results—circle points (empty: as measured on the pad, filled: as inferred for tip vicinity); blue solid curves—calculated based on M7 at plastic pads (dashed) and at tip vicinity. **a** For mode I fracture energy G_f and **b** for characteristic size (both normalized by values at zero crack parallel stress).

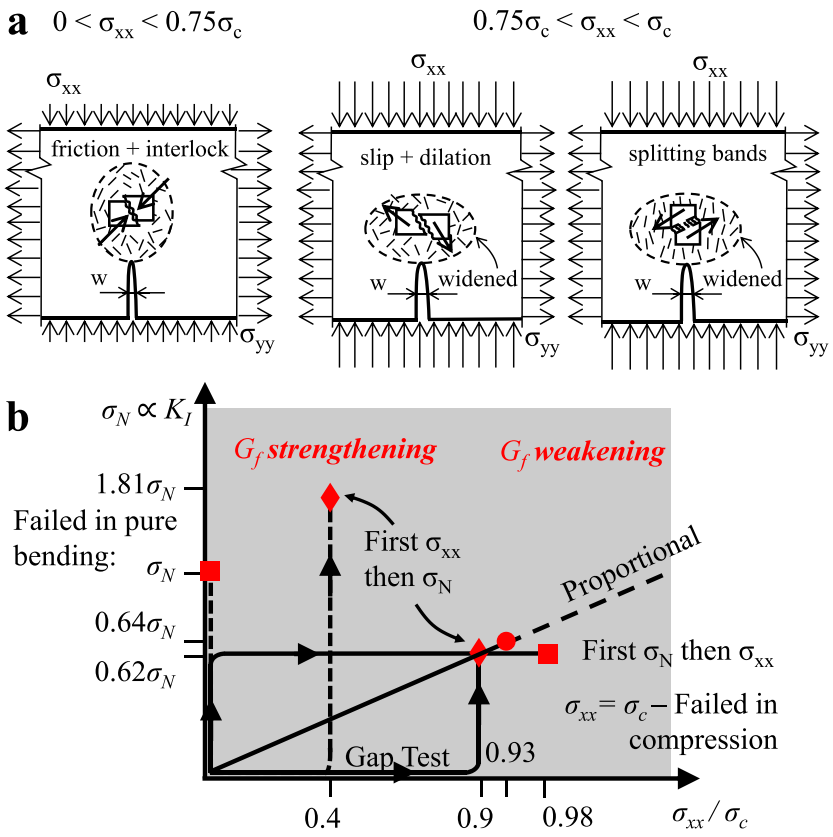

Fig. 3. a. Schematic of shape changes of the FPZ due to increasing σ_{xx}, with intuitive effects of microcrack friction and slip. **b.** Various loading paths leading to the same combination of crack-parallel stress σ_{xx} and the load, parametrized by applied nominal stress sig_N or by applied model I stress intensity factor K_I (note the enormous path dependence).

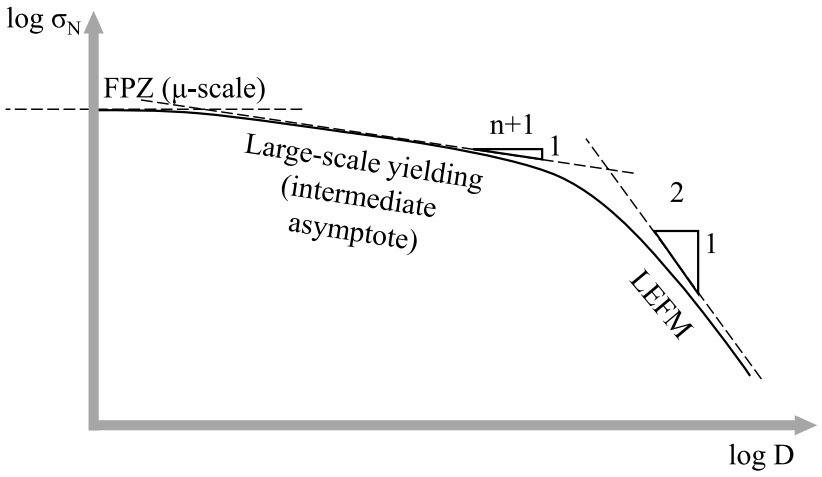

Fig. 4. Three asymptotic regimes of nominal strength in fracture of plastic-hardening metals, and schematic transitions between them.

transitions through three power-law regimes; see the straight lines in the log–log plot of nominal strength versus structure sizes in Fig. 4. An intermediate asymptote (a concept due to Barenblatt [25]) needs to be inserted between the small-size horizontal asymptote and the large-size asymptote of slope −1/2. Thus there are three transitional size effects to consider: from the first asymptote to the second, from the second to the third, and from the first to the third. The last one is practically most important and happens to have the same form as the original 1984 size effect law (SEL), but with parameters calculated differently.

The uniaxial stress–strain law of incompressible plastic-hardening metals can be taken in the Ramberg–Osgood [26] form: $\epsilon/\epsilon_y = \sigma/\sigma_y + \alpha_p(\sigma/\sigma_y)^n$, where σ_y = initial yield strength; ϵ_y = initial yield strain, α_p = empirical parameter; and n = plastic hardening exponent, typically 3 to 20 [4,5]. The tensorial generalization, in which the elastic strain is neglected [27], is written as [4,5,28,29]: $e_{ij} = (3\alpha_p\epsilon_y/2\sigma_y)(\sigma_{ef}/\sigma_y)^{n-1}s_{ij}$ where $\sigma_{ef} = (\frac{3}{2}s_{kl}s_{kl})^{1/2}$; here σ_{ef} is the scalar effective stress (the summation rule for repeated indices applies).

In the yielding zone, the near-tip field of displacement u_i, deviatoric stress s_{ij} and deviatoric strain e_{ij} $(i, j - 1, 2$, referred to Cartesian coordinates) has the separated form given by [4,5,8]:

$$u_i = \alpha_p\epsilon_y r_p(r/r_p)^{mn+1}F_i(\theta) \tag{1}$$

$$e_{ij} = \alpha_p\epsilon_y(r/r_p)^{mn}\varphi_{ij}(\theta), \quad s_{ij} = \sigma_y(r/r_p)^m\psi_{ij}(\theta) \tag{2}$$

where $\varphi_{ij}(\theta) = \frac{3}{2}\psi_{ij}(\theta)\left(\frac{3}{2}\psi_{kl}(\theta)\psi_{kl}(\theta)\right)^{\frac{n-1}{2}}$. Here (r,θ) are the polar coordinates centered at the crack tip, exponent m is a constant, and r_p is the effective size (or radius) of the yielding zone. The dimensionless angular functions F_i, ψ_{ij} and φ_{ij} are the solutions of ordinary differential equations, accurately calculated by the finite difference method [30,31], finite element method [32], or conformal mapping [33,34]. The energy flux through the yielding zone into the fracture process zone is calculated by Rice's path-independent J integral [35]:

$$J = \int_\Gamma \left(\bar{W}\,\mathrm{d}y - \nu_j\, s_{ij} u_{i,1}\mathrm{d}s\right), \quad \bar{W} = \int s_{ij}\mathrm{d}\epsilon_{ij} \tag{3}$$

where Γ is a closed contour around the fracture front, s is its length coordinate, ν_i its outward unit normal, and $y = x_2$, and $\bar{W}$ = strain energy density. With the help of the J-integral it has been shown [4,5,8] that

$$m = -\frac{1}{n+1} \tag{4}$$

For large-scale yielding in relatively small structures one gets the scaling laws (equivalent to Eqs. 5.3.10 in [28]):

$$u_i = \alpha_p \epsilon_y r_p (r/r_p)^{\frac{1}{n+1}} F_i(\theta) \tag{5}$$

$$e_{ij} = \alpha_p \epsilon_y (r/r_p)^{-\frac{n}{n+1}} \varphi_{ij}(\theta), \quad s_{ij} = \sigma_y (r/r_p)^{-\frac{1}{n+1}} \psi_{ij}(\theta) \tag{6}$$

It is normal to characterize the structural strength in terms of the nominal strength, $\sigma_N = P/bD$, where P is the applied load, b is the structure width (for a 2D structure), and D is the characteristic structure size. For large-scale yielding in small enough structures, one gets the size effect law:

$$\boxed{\sigma_N \propto \sigma_y \left(\frac{r_p}{D}\right)^{1/(n+1)}} \quad \text{(for large-scale yielding)} \tag{7}$$

Superposing the crack-parallel stress $\sigma_{xx} = T$ on the elastic singular stress field outside the yielding zone, one has

$$\sigma_{11}^{el} = (K_I/\sqrt{r}) f_{11}(\theta) + T \tag{8}$$

where $f_{11}(\theta)$ is a known function [36, p. 86]); $K_I = \sqrt{E'G_f}$ = mode I stress intensity factor, $E' = E$ (Young's modulus) and $E' - E/(1-\nu^2)$ for plain strain (ν = Poisson ratio). For small-scale yielding, the σ_{ij}^{el} field prevails at sufficiently large r, but for small r it interferes with the near-tip singular plastic-hardening field given by Eq. (6), i.e.,

$$\sigma_{ij}^{pl} = \sigma_y (r/r_p)^{-\frac{1}{n+1}} \psi_{ij}(\theta) \tag{9}$$

The fields in Eqs. (8) and (9) were optimally matched in Nguyen et al. [8] by virtual work equivalence preserving global equilibrium. After some calculations, this led to a simple equation for the effective radius r_p (or length $l_p = \zeta r_p$) of the plastic-hardening zone at crack front [8]:

$$\boxed{r_p = \frac{\kappa\, l_0}{(1 - \eta T/\sigma_y)^2}} \quad \text{where} \tag{10}$$

$$l_0 = \frac{E'G_f}{\sigma_y^2} = \frac{K_I^2}{\sigma_y^2}, \quad \kappa = \zeta^{-1}\left(\frac{C_e}{C_n C_p}\right)^2, \quad \eta = \frac{\pi}{C_n C_p} \tag{11}$$

$$C_n = \zeta^{-\frac{1}{(n+1)}} \frac{n+1}{2n+1}, \quad C_p = \int_{-\pi}^{\pi} \psi_{11}(\theta)\,\mathrm{d}\theta, \quad C_e = \frac{2}{3}\int_{-\pi}^{\pi} f_{11}(\theta)\,\mathrm{d}\theta \tag{12}$$

where l_0 = Irwin's material characteristic length. For the special case of $T = 0$, the foregoing expression is similar to Eq. (5.4-10) in [28] (except for the dimensionless factors C_n, C_p, C_e). Further note that, for the special case of $T = 0$, an estimate of r_p was obtained for an edge-notched tension specimen in a different way in 1976 by Shih and Hutchinson [12]).

The calculations given in [8] finally led to the large-scale size effect law for fracture of plastic-hardening metals describing the transit from the first to the final asymptote in Fig. 5:

$$\boxed{\sigma_N = \frac{\sigma_0}{\sqrt{1 + D/D_0}}} \tag{13}$$

which is applicable only if the smallest specimen depth is sufficiently larger than the yielding zone size (i.e., to the right of the intersection of the second and third asymptotes in Fig. 4).

The size effect law framed in Eq. (13) has the same form as the original (1984) size effect law for quasibrittle structures [14,37]. Its coefficients, however, are expressed differently:

$$\sigma_0^2 = E'G_f/2r_p + \sigma_p^2, \quad D_0 = 2r_p/g_0 \tag{14}$$

$$\sigma_p^2 = \frac{1}{2} E' \sigma_y \epsilon_y Q_p \tag{15}$$

Availability of this scaling law provides an alternative way to measure the fracture energy of metals, similar to that established for concrete (an international recommendation of RILEM [17], also endorsed by ACI-406). After obtaining the size effect data on notched specimens of sufficient size range (all of them sufficiently larger than the yielding zone), one needs to fit them optimally with Eq. (13), which is amenable to linear regression (Fig. 5c). Then one can solve G_f, r_p and σ_p from Eqs. (14) and (15).

Other scaling laws apply for the transitions from the first to the second, and the second to the third asymptote in Fig. 4; see [8].

3.1. Gap tests of aluminum and their size effect

Although the gap tests of aluminum beams of various sizes are still in progress at the time of writing, preliminary information can be given. The initial tests were already reported in [8] where also more information on the testing method was provided.

Three-point-bend (3PB) fracture specimens of aluminum (6061-T651) alloy have been tested at two levels of σ_{xx}. The experiments involved 4 different sizes with the size range of $1 : 2 : 4 : 8$ (corresponding to $D = 12, 24, 48, 96$ mm). The span-to-depth ratio was 4 and the initial notch depth was $a/D = 1/3$. All the dimensions were geometrically scaled in two dimensions except for the transverse thickness, $b = 10$ mm. A displacement-controlled procedure was used, with the rate of 0.002 mm/s for the smallest-size specimens. For larger sizes, the loading rate was scaled to preserve approximately the same strain rate on the crack-tip gage for all the sizes. The loading was run into the postpeak until the load dropped to 20% of the peak load due to bending.

The optimum fits of the available results obtained with Eq. (13) are presented in Fig. 5. G_f shows a 58% increase, corresponding to an expansion of the yielding zone.

4. Comments on reappraisal of fracture mechanics

Although the experimental studies and numerical simulations of fracture with crack-parallel stresses are still far from complete, the significant role of the crack-parallel stresses is already clear. It is now almost certain that the line crack models such as LEFM and CCM are inadequate for general applications unless it is known a priori that the crack-parallel stresses are, in the given situation, negligible. This also includes the XFEM, which is based on LEFM, and the phase-field models which uses a simplistic damage law with a single damage parameter (c, varying from 0 to 1) [38–41] (the "peridynamics" needs no comment; see [42]).

In practice, non-negligible crack-parallel stresses are ubiquitous:

1. The crack-parallel compression has been shown [43] to play a dominant role in the prediction of load capacity of reinforced concrete beams and slabs subjected to shear force loading. Five decades of attempts to predict the failure load with LEFM or CCM failed, because, as is now clear [43–45], the crack-parallel compression at peak load almost reaches the compression strength of concrete.

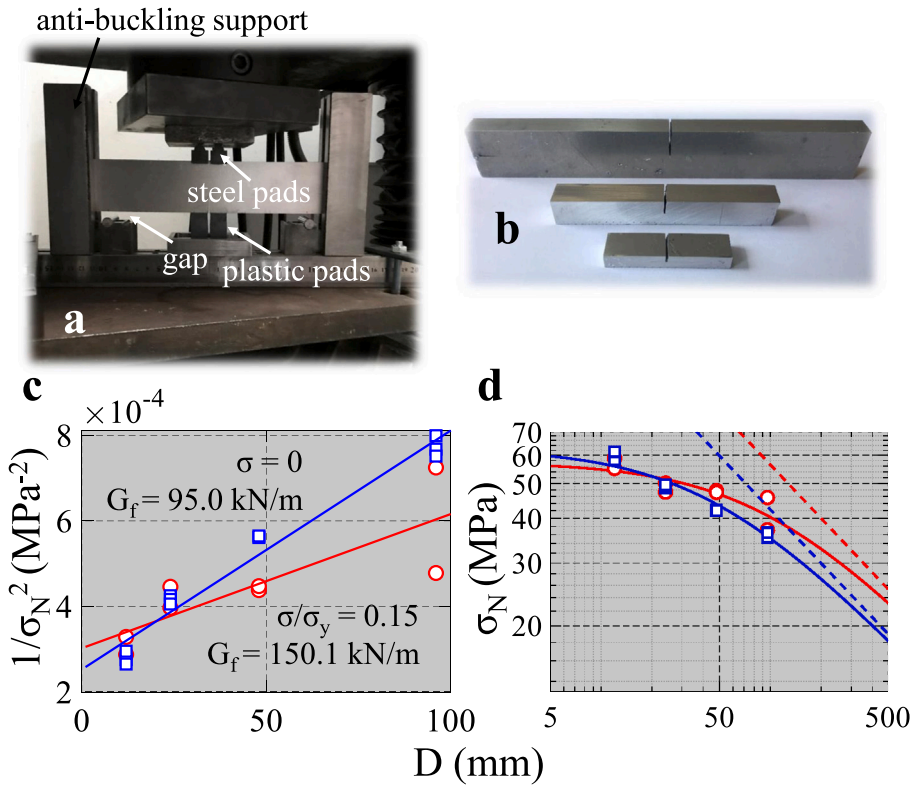

Fig. 5. **a.** Gap test setup for notched aluminum beam, showing beam of depth 96 mm and guard beams to prevent lateral buckling. **b.** Scaled notched aluminum beams of 3 sizes. **c.** Two linear regressions of size effect test results for two ratios of crack parallel stress σ_{xx}. **d.** Corresponding log–log size effect plots for the same two levels of σ_{xx}, with LEFM asymptotes of slope −1/2.

2. Seismic fractures of reinforced concrete columns of buildings or bridges are typically longitudinal or steeply inclined, with large crack-parallel compression.
3. So are most fractures in prestresed concrete.
4. The shear failure in the composite of aircraft wings, wing boxes, stabilizers or rudders is actually a tensile fracture with large crack-parallel compression.
5. A longitudinal crack in the pressurized composite fuselage is due to biaxial tension, with a large crack-parallel tension.
6. The longitudinal crack in the composite casing of a solid-fuel rocket occurs also under biaxial stress.
7. Ditto for fracture of various kinds of pressure vessels or inflatable shells.
8. The sideways cracks in unidirectional composites occur under large crack-parallel tension.
9. The hydraulic fracture of shale involves poromechanical stress transfer from the fluid to the solid phase, and is surely affected by tectonic and overburden stresses along the fracture.
10. The tectonic stress parallel to a propagating earthquake fault must play a role at the fault front.
11. Crack-parallel compression acts in most fractures of sea ice, either propagating longitudinally, as in ice sheets pushing against the legs of an oil platform, on transversely, as under vertical load.
12. The composite crush cans, enhancing crashworthiness of automobiles, fracture longitudinally under a large crack-parallel compression.
13. So do the cracks produced in concrete walls under projectile impact.
14. Most thermal cracks in metals or drying cracks in concrete or soil occur under biaxial tension.
15. Microcracks in MEMS evolve under biaxial stresses, too.
16. Although not yet investigated, it is likely that the crack-parallel stresses also change the prefactors of the Paris law and Charles-Evans law for cyclic and static fatigue in metals and composites.

Finally, it should be emphasized that, to capture the effects of crack-parallel stresses, fracture must be modeled as a band of *finite width* at the crack front, and with a tensorial softening damage constitutive model that can reproduce *oriented* microcrack or slips on the meso-level.

Declaration of competing interest

The authors declare that they have no known competing financial interests or personal relationships that could have appeared to influence the work reported in this paper.

Acknowledgment

Partial preliminary funding under NSF Grant CMMI-1439960 to Northwestern University is gratefully acknowledged.

References

[1] Tschegg EK, Elser M, Stanzl-Tschegg SE. Biaxial fracture tests on concrete—Development and experience. Cem Concr Compos 1995;17:57–75.
[2] Nguyen Hoang, Pathirage M, Rezaei, Issa M, Cusatis G, Bažant ZP. New perspective of fracture mechanics inspired by gap test with crack-parallel compression. Proc Natl Acad Sci 2020;117(25):14015–20.
[3] Nguyen Hoang, Pathirage M, Cusatis G, Bažant ZP. Gap test of crack-parallel stress effect on quasibrittle fracture and its consequences. J Appl Mech 2020;87(7).
[4] Hutchinson JW. Singular behaviour at the end of a tensile crack in a hardening material. J Mech Phys Solids 1968;16(1):13–31.
[5] Rice J, Rosengren GF. Plane strain deformation near a crack tip in a power-law hardening material. J Mech Phys Solids 1968;16(1):1–12.

[6] O'dowd NP, Shih CF. Family of crack-tip fields characterized by a triaxiality parameter—I. Structure of fields. J Mech Phys Solids 1991;39(8):989–1015.
[7] O'Dowd NP, Shih CF. Family of crack-tip fields characterized by a triaxiality parameter—II. Fracture applications. J Mech Phys Solids 1992;40(5):939–63.
[8] Nguyen Hoang T, Dönmez AA, Bažant ZP. Structural strength scaling law for fracture of plastic-hardening metals and testing of fracture properties. Extrem Mech Lett 2021;43:101141.
[9] Stanzl-Tschegg SE, Tan D-M, Tschegg EK. New splitting method for wood fracture characterization. Wood Sci Technol 1995;29(1):31–50.
[10] Betegón C, Hancock JW. Two-parameter characterization of elastic-plastic crack-tip fields. J Appl Mech 1991;58(1):104–10.
[11] Gao X, Shih C, Tvergaard V, Needleman A. Constraint effects on the ductile-brittle transition in small scale yielding. J Mech Phys Solids 1996;44(8):1255–82.
[12] Shih CF, Hutchinson JW. Fully plastic solutions and large scale yielding estimates for plane stress crack problems. J Eng Mater Technol 1976;98:289–95.
[13] Cotterell B, Rice JR. Slightly curved or kinked cracks. Int J Fract 1980;16:155–69.
[14] Bažant ZP, Kazemi MT. Size effect in fracture of ceramics and its use to determine fracture energy and effective process zone length. J Am Ceram Soc 1990;73:1841–53.
[15] Hoover CG, Bažant ZP. Cohesive crack, size effect, crack band and work-of-fracture models compared to comprehensive concrete fracture tests. Int J Fract 2014;187:133–43.
[16] Bažant ZP, Kazemi MT. Size effect on diagonal shear failure of beams without stirrups. ACI Struct J 1991;88(3):268–76.
[17] RILEM Recommendation TC89-FMT. Size-effect method for determining fracture energy and process zone size of concrete. Mater Struct 1990;23(6):461–5.
[18] Bažant Zdeněk P, Oh Byung H. Microplane model for progressive fracture of concrete and rock. J Eng Mech 1985;111(4):559–82.
[19] Bažant ZP, Planas J. Fracture and size effect in concrete and other quasibrittle materials. Boca Raton, FL: CRC Press; 1998.
[20] Červenka J, Bažant ZP, Wierer M. Equivalent localization element for crack band approach to mesh-sensitivity in microplane model. Int J Numer Meth Eng 2005;62(5):700–26.
[21] Caner FC, Bažant ZP. Microplane model M7 for plain concrete. I: Formulation. J Eng Mech 2013;139:1714–23.
[22] Caner FC, Bažant ZP. Microplane model M7 for plain concrete. II: Calibration and verification. J Eng Mech 2013;139:1724–35.
[23] Bažant ZP, Schell WF. Fatigue fracture of high-strength concrete and size effect. ACI Mater J 1993;90:472.
[24] Bažant ZP, Xiang Yuyin. Size effect in compression fracture: splitting crack band propagation. J Eng Mech 1997;123:162–72.
[25] Barenblatt GI. Similarity, self-similarity, and intermediate asymptotics. New York: Consultants Bureau; 1979.
[26] Ramberg W, Osgood WR. Description of stress-strain curves by three parameters. In: Technical note 902. Washington, D.C.: NACA; 1943.
[27] Hutchinson JW, Paris PC. Stability analysis of J-controlled crack growth. In: Elastic-plastic fracture. ASTM International; 1979.
[28] Kanninen MF, C.H. Popelar. Advanced fracture mechanics. Oxford engineering science series, New York: Oxford University Press; 1985.
[29] Anderson TL. Fracture mechanics: fundamentals and applications. Boca Raton, FL: CRC Press; 1991.
[30] Rice JR. Mathematical analysis in the mechanics of fracture. In: Fracture: an advanced treatise, Vol. 2. 1968, p. 191–311.
[31] Nikishkov GP. J-a fracture concept based on the three-term elastic-plastic asymptotic expansion of the near-crack tip stress field. In: Fracture: A topical encyclopedia of current knowledge. Citeseer; 1998, p. 557–74.
[32] Levy N, Marcal PV, Ostergren WJ, Rice JR. Small scale yielding near a crack in plane strain: a finite element analysis. Int J Fract Mech 1971;7(2):143–56.
[33] Revil-Baudard B, Cazacu O, Chandola N. Effect of the yield stresses in uniaxial tension and pure shear on the size of the plastic zone near a crack. Int J Plast 2018;102:101–17.
[34] Xin Gao, Hangong Wang, Xingwu Kang, Liangzhou Jiang. Analytic solutions to crack tip plastic zone under various loading conditions. Eur J Mech A Solids 2010;29(4):738–45.
[35] Rice JR. A path independent integral and the approximate analysis of strain concentration by notches and cracks. ASME J Appl Mech 1968;35(2):379–86.
[36] Bažant ZP, Planas J. Fracture and size effect in concrete and other quasibrittle materials. New directions in civil engineering, Boca Raton, New York: CRC Press; 1998.
[37] Bažant ZP. Mechanics of fracture and progressive cracking in concrete structures. Boston: Springer Netherlands; 1985, p. 1–94.
[38] Moës N, Dolbow J, Belytschko T. A finite element method for crack growth without remeshing. Internat J Numer Methods Engrg 1999;46(1):131–50.
[39] Bourdin B, Francfort GA, Marigo J-J. Numerical experiments in revisited brittle fracture. J Mech Phys Solids 2000;48(4):797–826.
[40] Bourdin B, Francfort GA, Marigo J-J. The variational approach to fracture. J Elasticity 2008;91(1–3):5–148.
[41] Borden MJ, Verhoosel CV, Scott MA, Hughes TJ R, Landis CM. A phase-field description of dynamic brittle fracture. Comput Meth Appl Mech Engrg 2012;217:77–95.
[42] Bažant ZP, Luo Wen, Chau VT, Bessa MA. Wave dispersion and basic concepts of peridynamics compared to classical nonlocal damage models. J Appl Mech 2016;83.
[43] Dönmez A, Bažant ZP. Critique of critical shear crack theory for fib model code articles on shear strength and size effect of reinforced concrete beams. Struct Conc 2019;20(4):1451–63.
[44] Dönmez A A, Carloni C, Cusatis G, Bažant ZP. Size effect on shear strength of reinforced concrete: Is CSCT or MCFT a viable alternative to energy-based design code? J Eng Mech 2020;146(10).
[45] Dönmez A, Carloni C, Cusatis G, Bažant ZP. Discussion of the article "From experimental evidence to mechanical modeling and design expressions: The critical shear crack theory for shear design". Struct Concr 2020;21(4):1688–9.